Determination of dipole and quadrupole polarizabilities of Ba^+ by measurement of the fine structure of high-L $n=9$ and 10 Rydberg states of barium

E. L. Snow, M. A. Gearba, R. A. Komara, and S. R. Lundeen
Department of Physics, Colorado State University, Fort Collins, Colorado 80523, USA

W. G. Sturrus
Department of Physics, Youngstown State University, Youngstown, Ohio 44555, USA
(Received 19 October 2004; published 25 February 2005)

The fine structure of high-angular-momentum $n=9$ and 10 Rydberg states of barium has been measured precisely, using the resonant excitation Stark ionization spectroscopy method. Optical transitions corresponding to $(n,n')=(10,30)$, (9,17), and (9,20) were induced with a Doppler-tuned CO_2 laser, determining the fine-structure energies corresponding to all $n=9$ and 10 levels with $L\geqslant 6$. The pattern of these fine-structure energies conforms closely with an effective potential model, by comparison with which the dipole and quadrupole polarizabilities of Ba^+ can be determined. Combining our data with earlier measurements made it possible to deduce, in addition, the portion of α_2 due to the lowest excited D state of Ba^+. Our best estimates of these three properties are $\alpha_1=124.30(16)a_0^3$, $\alpha_2=2462(361)a_0^5$, and $\alpha_2^0=1828(88)a_0^5$.

DOI: 10.1103/PhysRevA.71.022510 PACS number(s): 32.10.Dk, 32.10.Fn, 32.30.Bv

I. INTRODUCTION

The fine-structure patterns in nonpenetrating high-L Rydberg states provide a unique signature of interactions between the Rydberg electron and the positive ion core that break the symmetry of the dominant simple Coulomb potential. Measurements of these patterns can provide precise determinations of the core properties such as dipole polarizability and quadrupole moments, which control these interactions and so set the scale of the fine-structure patterns. Achieving this requires measurements in a wide enough range of L's to establish the fine-structure pattern clearly and in states with large enough L, typically $L\geqslant 5$, so that complications due to core penetration can be neglected. Successful studies of this type have been carried out previously in the neon atom [1] and the H_2 and D_2 molecules [2,3] using the resonant excitation Stark ionization spectroscopy (RESIS) microwave method, resulting in determinations of the dipole polarizabilities and quadrupole moments of the core ions. More recently, the same approach has been used to determine the polarizability of the Na-like ion Si^{3+} [4] and the Mg-like ion Si^{2+} [5] by measuring the fine-structure pattern in high-L Rydberg states with these ion cores. The RESIS technique provides a general method of accessing the high-angular-momentum levels that are required for such studies. With this method, the Rydberg atoms, molecules, or ions are formed by single-electron capture from an accelerated ion beam. All possible angular momentum states are formed at some level in this process. Specific high-L Rydberg levels in the resulting fast beam can be detected by upward excitation using a Doppler-tuned CO_2 laser followed by Stark ionization of the upper state of the excitation and collection of the resulting ions. The fact that the laser excitation is upwards from existing levels means that all angular momentum states are eligible to be detected in this way, and as long as the fine-structure energies exceed the laser resolution, individual Rydberg levels can be selectively detected. In most past studies, the relatively small fine-structure intervals have been measured directly using microwave resonance methods, relying on the selective RESIS excitation to provide detection of those transitions [1–5]. In other cases, the fine-structure energies have been large enough that simply measuring the frequencies of the RESIS transitions was sufficient to determine the fine-structure energies at an interesting level of precision [6–8]. The existence of these high-L fine-structure patterns, coupled with a practical and general method of studying them, provides a versatile tool for measuring certain properties of positive ions that is, in some ways, superior to methods available for the study of neutral atom properties [5].

One of the most interesting ions whose properties could be studied with these techniques is the Ba^+ ion. The alkali-metal atoms Cs and Fr and the alkali-like ions Ba^+ and Ra^+ are among the best candidates for precise atomic tests of parity violating weak interactions. The most successful measurements to date have been carried out in Cs [9], but measurements are being actively pursued in Fr [10] and Ba^+ [11]. In each case, however, achieving a precise test of standard model predictions requires, in addition to the experimental measurements, a reliable understanding of the atomic-structure matrix elements that connect the measured quantities to fundamental interaction strengths. In Cs, a comparison of measurements and calculations of a number of related atomic properties have been examined to estimate the precision of the matrix elements. In that case, the precision of the calculations appears to be about 0.4% and is the limiting factor in comparing PNC measurements to standard model predictions [9]. Among the atomic properties which can be compared with calculations at this level of precision are excited state lifetimes, hyperfine constants, and polarizabilities or Stark-shift rates. In the case of Fr, recent experiments now test properties similar to those studied in Cs with similar precision [12–14]. In Ba^+, however, although calculations have been carried out with similar care [15], there are far

fewer precise experimental tests. For example, the lifetime of $6P$ states in Ba^+ has been measured only to a precision of about 1.3% [16]. Therefore a precise measurement of the ground-state polarizability of Ba^+ by means of the spectroscopy of Rydberg states of barium would be a significant additional test of the theory of this significant ion.

Rydberg states of the barium atom have been studied previously by Gallagher and co-workers [17]. In one of the earliest examples of high-L Rydberg spectroscopy, they determined the fine structure intervals between $6snl$-$6snl'$ with $l=4$–7 states and $n=18$–23. Analysis of the level structure was complicated by the large nonadiabatic contributions to the structure, but they were still able to obtain the first measurements of the dipole and quadrupole polarizabilities of the Ba^+ ground state, $\alpha_1=125.5(1.0)a_0^3$ and $\alpha_2=2050(100)a_0^5$. This work extends that study to include a range of higher-L levels within the $n=9$ and 10 levels of barium. Our conclusions confirm the earlier result for α_1 with increased precision. We find a somewhat larger value of α_2 and also resolve separately the contribution to α_2 from the lowest excited D state of the Ba^+ core. The extended data pattern also confirms the significant nonadiabatic effects that occur in this system, even in states with $L>5$. In addition, the present study provides additional measurements of spin-doublet splittings first observed in barium Rydberg states in the study of Gallagher *et al.* [17] and later given a theoretical explanation by Snow *et al.* [18].

The barium Rydberg states described here are almost without exception all $6snl$ states with total angular momentum $L=$l. For simplicity we will denote the state by n and L, abbreviating the total angular momentum L with standard spectroscopic notation, i.e., S,P,D,F,G,H ($L=5$), I ($L=6$), K ($L=7$), L ($L=8$), M ($L=9$), and N ($L=10$). Although convenient, this notation is potentially confusing, especially when the symbol L is used to denote the specific value 8 rather than the total angular momentum. The distinction should, however, be clear from the context.

II. EXPERIMENT

The fine structure of barium Rydberg levels is studied here by measuring the frequencies of the RESIS excitation transitions and comparing them with hydrogenic frequencies. Transitions exciting $n=10$ Rydberg levels to $n=30$ and $n=9$ Rydberg levels to $n=17$ or 20 are close enough to the frequencies of discrete CO_2 laser lines that they can be Doppler tuned into resonance by varying the angle of intersection between the CO_2 laser and the fast barium beam. The resonance angle is measured precisely and used to deduce the resonance frequency, using independent measurements of the beam velocity. The difference of this transition frequency from a purely hydrogenic transition is due to the fine-structure energies of both the upper and lower states of the transition, but most of the contribution comes from the lower state. Thus the measurements essentially determine the fine-structure energies of high-L $n=9$ and 10 Rydberg states. These can be compared with an effective potential model to determine the dipole and quadrupole polarizabilities of Ba^+.

The schematic of the apparatus used in this work is shown in Fig. 1. A 9.5-keV ion beam is created in a Colutron model-101 ion source, and the Ba^+ ion is selected by use of a $\boldsymbol{v}\times\boldsymbol{B}$ velocity filter. The ions are then collided with a selectively excited 8F/9D Rb target [6]. Depending on the target conditions, charge transfer occurs for 0.5%–2% of the ion beam. When charge transfer of a single electron takes place, the binding energy of the electron tends to remain constant. This creates a fast neutral barium beam with a population centered about $n=8$ and with a significant fraction in $n=9$ and 10. States of $n=15$ and higher are then Stark ionized in the initial stripper and deflected with the remaining Ba^+ ions. This allows only the states with $n<15$ to enter the CO_2 laser interaction region. Here a Doppler-tuned CO_2 laser excites a particular transition to a higher state of neutral barium. These higher states are then Stark ionized in the stripper, and the resulting Ba^+ ions are collected. Figure 2 shows data from a typical RESIS signal, the $10L$-$30M$ transition of barium. The ionization current collected in the detector is plotted versus

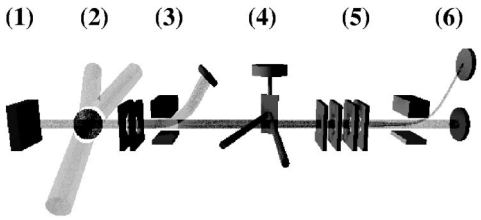

FIG. 1. Schematic diagram of the optical RESIS apparatus used for this study. (1) A Ba^+ ion beam is created in a Colutron model-101 ion source. The ions are then collided with a selectively excited $8F/9D$ Rb target at (2) where some ions capture an electron. States of $n=15$ and higher are then Stark ionized in the initial stripper and deflected with the remaining Ba^+ ions at (3) to be collected in a Faraday cup. Neutral barium atoms with $n<15$ enter the CO_2 laser interaction region (4). Here a Doppler-tuned CO_2 laser excites a particular transition to a higher state of neutral barium for example $n=10$ atoms might be excited to $n=30$. The excited states are then Stark ionized in the stripper and focused by the lens at (5) and the resulting Ba^+ ions are deflected collected on a channeltron plate at (6) while the neutral beam continues straight and is collected in a Faraday cup.

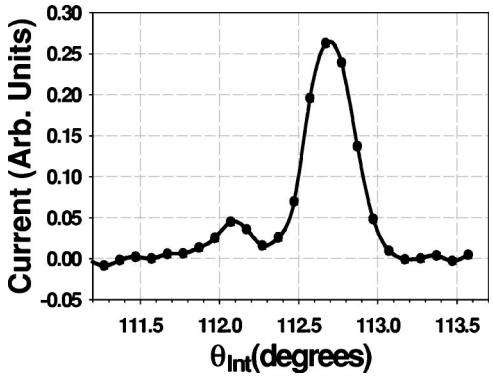

FIG. 2. Measured ionization current using RESIS optical method vs the intersection angle of the Doppler-tuned CO_2 laser. The large peak is the barium $10L$-$30M$ transition. The peak at smaller intersection angle is the Stark admixed, $\Delta L=2$, $10L$-$30N$ transition, whose relative amplitude can be used to determine the amount of stray electric field present in the laser interaction region.

TABLE I. Measured transitions listed with the number of times observed, the CO_2 laser frequency, the experimental intersection angle for ^{138}Ba corrected for influence of other barium isotopes, the corresponding frequency corrected for the Stark-shift contributions, and the difference of this frequency from a purely hydrogenic transition.

nL-$n'L'$	No. of observations	Laser frequency (cm^{-1})	θ_{Int} (°)	ν^0 (cm^{-1})	ν^0-hydrogenic (cm^{-1})
(9*I*-17*K*)*a*	2	977.2139(2)	131.685(94)	976.9646(3)	1.9007(3)
(9*I*-17*K*)*b*	2	977.2139(2)	127.187(92)	976.9873(4)	1.9234(4)
(9*K*-20*L*)*a*	2	1081.0874(2)	57.806(84)	1081.3083(4)	0.8742(4)
(9*K*-20*L*)*b*	2	1081.0874(2)	57.135(84)	1081.3126(4)	0.8785(4)
(9*L*-20*M*)	3	1081.0874(2)	123.900(77)	1080.8561(3)	0.4220(3)
(10*I*-30*K*)*a*	4	977.2139(2)	129.168(79)	976.9777(3)	1.5388(3)
(10*I*-30*K*)*b*	4	977.2139(2)	125.130(78)	976.9988(3)	1.5599(3)
(10*K*-30*L*)*a*	2	975.9304(2)	56.223(83)	976.1386(4)	0.6997(4)
(10*K*-30*L*)*b*	2	975.9304(2)	55.605(95)	976.1420(4)	0.7031(4)
(10*L*-30*M*)	2	975.9304(2)	112.736(77)	975.7859(4)	0.3470(4)
(10*M*-30*N*)	1	975.9304(2)	145.804(116)	975.6212(5)	0.1823(5)

the Doppler-tuned intersection angle of the CO_2 laser. The angular width of the resonance, about 0.30°, is determined jointly by the transit time through the CO_2 laser and by the collimation of the barium beam ($\approx 0.20^{\circ}$). Resonance curves such as Fig. 2 were fit to determine the resonance angle with a typical precision of 0.02°.

The large size of the barium fine structure combined with the limited Doppler tuning range of the CO_2 laser determined which barium lines can be observed. The speed of the barium beam limits the tuning range to less than 0.04% of the CO_2 laser line frequency, or about 0.38 cm^{-1}. Since the separation between CO_2 laser lines is about 2 cm^{-1}, this leaves some frequencies unavailable. Listed in Table I are the measured barium transitions, the CO_2 laser lines used to observe them, and the intersection angle at which they were observed. Some of these transitions have doublet splittings, and in these cases two positions are given. The quoted intersection angle is measured with respect to the beam axis, with zero degrees representing laser propagation directly into the barium beam. The calibration procedure used to determine the intersection angle from experimental measurements is described below. Also shown in Table I are the values of the Doppler-tuned laser frequencies corresponding to each transition, again obtained by use of the calibration procedure described below, and the differences of these frequencies from the corresponding hydrogenic transition frequencies, which are taken to be

$$\Delta\upsilon_{Hyd} = 109\,736.877\ \mathrm{cm}^{-1}\left[\frac{1}{n_L^2} - \frac{1}{n_U^2}\right], \tag{1}$$

where n_U and n_L are the principal quantum numbers of the upper and lower states of the RESIS transition.

As seen in Fig. 1, the Doppler tuning of the CO_2 laser is accomplished with a single mirror mounted on a rotation stage. The laser enters the region through a ZnSe window, intersecting the beam initially at approximately 90° and then reflecting off the mirror to intersect the beam a second time at an angle controlled by the setting of the stage. The angle of intersection is given by

$$\theta_{Int} = 90 - 2(\theta_{stage} - \theta_{perp}), \tag{2}$$

where θ_{stage} is the reading of the rotation stage, which *per se* has no significance since it contains an arbitrary offset, and θ_{perp} is the reading of the rotation stage at which the reflected laser beam intersects the Ba beam at exactly 90°. The value of θ_{perp} must be determined carefully by calibration measurements in order to convert the recorded stage angle reading to an actual intersection angle. This single-reflection rotation stage is a simpler design than has been used in previous RESIS measurements [8].

Calibration of this system was performed by inducing analogous transitions in the helium atom whose frequencies have been calculated to high precision. The speed of the helium beam at 9.5 keV is an order of magnitude faster than the barium beam and as a result these transitions can be measured with multiple CO_2 laser lines at different Doppler-tuned angles. Numerous observations of these helium transitions can be fit with unique values of β and θ_{perp} to the following relation, which translates the stage angle to a frequency:

$$\nu' = \frac{\nu_L}{\sqrt{1-\beta^2}}\{1 + \beta \sin[2(\theta_{stage} - \theta_{perp})]\}, \tag{3}$$

where ν' is the transition frequency, ν_L is the frequency of the laser line, and $\beta = \upsilon/c$. The frequencies of the CO_2 laser lines, ν_L, are taken from a standard reference [19] and are manually maintained within ±10 MHz of the center of the gain profile. Listed in Table II are the helium transition frequencies, obtained from the calculations of Drake [20]. Also given are the stage angles at which these transitions were observed, the CO_2 line used in the observation, the stage angles predicted from the fit to Eq. (3), and the difference of the observed angle from that predicted by the best fit. The difference of the fit from the accepted values has a root mean

TABLE II. Helium calibration transitions listed with the calculated frequency, the laser frequency used, the observed stage angle, the fitted angle predicted from Eq. (3), and difference of the observed angle from the fit.

nL-nL′	Calc. freq. (cm^{-1})	Laser freq. (cm^{-1})	Obs. angle (°)	Fitted angle (°)	Obs.-fit (°)
10*F*-30*G*	975.4016	977.2139	155.880(17)	155.823	0.057
10*F*-30*G*	975.4016	975.9304	176.552(5)	176.603	−0.051
10*F*-30*G*	975.4016	975.9304	176.580(4)	176.603	−0.023
10*F*-30*G*	975.4016	974.6219	193.914(11)	193.967	−0.053
10*F*-30*G*	975.4016	974.6219	193.915(13)	193.967	−0.052
10*F*-29*G*	966.8487	966.2504	191.543(20)	191.509	0.034
10*F*-29*G*	966.8487	967.7072	171.910(5)	171.927	−0.017
10*F*-27*G*	946.8042	947.7420	170.552(8)	170.493	0.059
10*F*-27*G*	946.8042	945.9802	194.963(5)	194.904	0.058
10*G*-27*H*	946.7372	947.7420	169.511(3)	169.481	0.030
10*G*-27*H*	946.7372	945.9802	193.902(17)	193.934	−0.032
9*G*-17*H*	979.9665	974.6219	188.091(8)	188.080	0.011
9*G*-17*H*	979.9665	975.9304	170.543(9)	170.555	−0.012
9*G*-20*H*	1080.3235	1078.5906	206.268(18)	206.306	−0.039
9*G*-20*H*	1080.3235	1081.0874	174.420(6)	174.420	0.000
9*F*-17*G*	975.0555	974.6219	189.284(8)	189.261	0.023
9*F*-17*G*	975.0555	975.9304	171.818(8)	171.834	−0.016
9*F*-20*G*	1080.4139	1081.0874	175.525(5)	175.534	−0.009
9*F*-20*G*	1080.4139	1081.0874	175.491(9)	175.534	−0.043
9*F*-20*G*	1080.4139	1078.5906	207.884(22)	207.869	0.015
Second run					
10*F*-30*G*	975.4016	977.2139	155.789(14)	155.783	0.006
10*F*-30*G*	975.4016	977.2139	155.775(9)	155.783	−0.008
10*F*-30*G*	975.4016	975.9304	176.6462(5)	176.579	0.067
10*F*-30*G*	975.4016	975.9304	176.630(5)	176.579	0.051
10*F*-30*G*	975.4016	974.6219	193.948(4)	193.951	−0.003
10*F*-30*G*	975.4016	974.6219	193.963(5)	193.951	0.012
9*F*-17*G*	975.0555	974.6219	189.227(10)	189.243	−0.016
9*F*-17*G*	975.0555	974.6219	189.245(3)	189.243	0.002
9*F*-17*G*	975.0555	975.9304	171.783(3)	171.807	−0.024
9*F*-20*G*	1080.4139	1081.0874	175.491(4)	175.509	−0.019
9*F*-20*G*	1080.4139	1078.5906	207.856(4)	207.864	−0.008

square of 0.034°. This calibration procedure was repeated following two separate data runs measuring the barium RESIS transitions, and consistent results were found in the two calibrations. However, it was observed that the scatter in the observed helium resonance angular positions was somewhat larger than the statistical errors obtained in fits of the resonance lines. The limiting error in the calibration appears to be the pointing stability of the barium beam. This was collimated to a full width of about 0.20°. It appears that variations in the average angular position of the barium beam within this 0.20° window are responsible for the 0.034° rms scatter in the calibration fit. Examination of the time correlation of the fit residuals indicates that the pointing stability error is approximately random, so we attach this statistical error to the best value of θ_{perp} determined from the calibration fits. This proves to be the most significant source of experimental error in determining the barium RESIS transition frequencies. The best values of θ_{perp} and β for the helium calibration runs were found to be

$$\beta_{He} = 0.002\,251\,6(12),$$

$$\theta_{perp} = 183.587(34).$$

The fitted value of β_{He} corresponds to a kinetic energy of 9.449(13) keV, in approximate agreement with the nominal 9.50 keV acceleration voltage.

The value of θ_{perp} is the same for both helium and barium. The acceleration voltage of the ion source also remains the same for both ions. Thus the speed of the barium beam is

simply the square root of the mass ratio times the speed of the helium beam. Because the mass resolution of our velocity filter is $\Delta m/m=0.04$, all barium ions are present in the ion beam at their natural abundance. However, because of their different speeds due to the different masses, the RESIS signals are partially resolved. Simulations show that the center of the composite RESIS signal is very close to the position expected for a pure ^{138}Ba beam, the most abundant isotope (72%). The mass of the $^{138}Ba^{+}$ ion is 137.9050 amu and the He^{+} ion has a mass of 4.002 055 amu, giving $\beta_{Ba}=0.000\,383\,6(21)$. This was used to convert the fitted stage angle positions to the Doppler-shifted frequencies given in Table I. A small systematic correction, less than 0.0003 cm^{-1}, was applied to account for the residual influence of the other barium isotopes.

Only one other systematic correction was applied to obtain the results shown in Table I. As seen in previous RESIS experiments, static electric fields can build up over time in the laser interaction region. Magnetic shielding was used in this region to eliminate motional fields due to the Earth's magnetic field. Still significant electric fields build up due to the charging of nominally conducting surfaces. Stark effects from these electric fields cause frequency shifts in the transitions and Stark mixing of adjacent levels, which begin to allow forbidden $\Delta L=0$ or 2 transitions. Stark-shift rates can be calculated for each of the upper states from approximate knowledge of the dipole polarizability. Also, observations of normally forbidden $\Delta L=0$ or 2 transitions, such as the $\Delta L=2$ transition shown in Fig. 2, can be used to estimate the strength of ambient stray fields. The ratio of forbidden to allowed transition amplitudes is assumed to be proportional to the square of the wave function admixture, which in turn can be related to the ambient stray field by theory of the Stark effect [8]. The estimated fields ranged from 0.05 V/cm to 0.17 V/cm. The Stark shifts produced by fields of this size are not large. They are most significant for the transitions where the upper state is $n=30$, and in this case, corrections as large as 0.0005 cm^{-1} were applied. The error bar for each transition was expanded by half the applied Stark-shift correction, and these errors are included in the last two columns of Table I.

III. ANALYSIS

A. Spin splittings

The transitions originating in $L=6$ and $L=7$ states exhibit a spin splitting which is much larger than the Dirac spin-orbit splitting, whose magnitude might be expected to approximate the spin splitting in these states. Similar splittings were observed in the previous study by Gallagher *et al.* [17] and were recently attributed to an "indirect spin-orbit" effect due to admixtures of excited P and D states into the nominally S-state ion core [18]. The new observations here significantly extend the data pattern of observed barium spin splittings. Figure 3 illustrates that pattern. The square points are the ratios of the previously observed splittings in $18\leqslant n\leqslant 23$, $L=5$, 6, and 7 levels [17], normalized to the naïve Dirac spin-orbit splittings [18]. The triangular points show the later measurements of Vassen *et al.* in $L=5$ levels [21]. The round points show the splittings of the $L=6$ and 7 levels in $n=9$ and 10 measured in this study. The dashed lines show the theoretical predictions using the model of the indirect spin-orbit splittings presented earlier [18]. The model shows very good agreement with the measurements in $L=7$ levels, across a wide range of n. The agreement is poorer in the $L=6$ levels, especially at high n. We believe this is due to the poorer convergence of the adiabatic expansion, which is assumed in deriving the indirect spin orbit model [18] in the $L=6$ levels. This is closely related to the comparison between measured $L=6$ fine-structure intervals and the effective potential model, discussed in more detail below. The apparently good agreement between the spin splitting model and high n measurements in $L=5$ levels is, we believe, fortuitous, since the convergence of the adiabatic expansion is even worse in these levels. This is confirmed by the increasingly poor agreement with measurements in lower-n, $L=5$ levels. These show the influence of strong quadrupole mixing with the $5d4f$ level which occurs near the $6s10h$ level [21]. Table III lists the new splittings measured here along with the predicted splittings obtained from the indirect spin-orbit model.

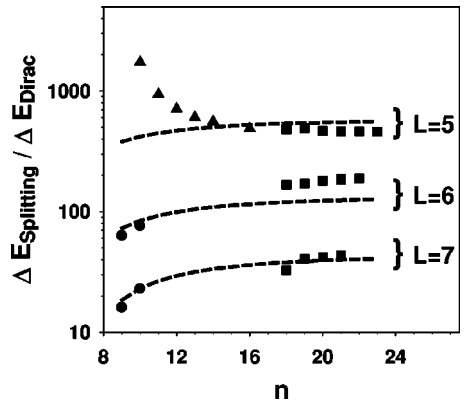

FIG. 3. Observed spin splittings for several $L=5$, 6, and 7 states divided by the Dirac spin-orbit calculated for each state. Previous measurements by Gallagher *et al.* [17] are given plotted as square points. Measurements performed by Vassen *et al.* [21] are given as triangles. The current measurements are shown as circles and the lines are the predictions based on the indirect spin orbit model [18] with $\alpha_1=124.30$ and $\alpha_2^0=1828$.

B. Fine-structure intervals

The level of agreement between the observed and predicted spin splittings is sufficient so that the interval between the centers of gravity of the spin doublets can be accurately deduced with the use of this theory. The two observed transition energies are transitions between corresponding levels in the two states, either between $K=L+1/2$ states or between $K=L-1/2$ states, where K is the total angular momentum exclusive of Rydberg-electron spin. According to the indirect spin-orbit model, the state with higher K has the higher energy and the splitting in n_U is much smaller than the splitting in n_L. Therefore the higher transition energy $h\nu_+$ comes from the states with $K=L-1/2$, and an expression for the interval between the center of gravity of the two spin doublets is

TABLE III. The difference of the observed frequency to the purely hydrogenic transitions is given in column 2. ΔE_{FS}, listed for each measured transitions in column 3, is the interval between the centers of gravity of each doublet minus the hydrogenic energy. The splitting ΔE_{spin} is the observed splitting of the measured transition. The final column gives the predictions of the indirect spin-orbit theory for the measured transitions.

nL-$n'L'$	ν^0- hyd (cm^{-1})	ΔE_{FS} (cm^{-1})	ΔE_{spin} (cm^{-1})	ΔE_{spin} predicted (cm^{-1})
9*I*-17*K*	1.9007(3)			
	1.9234(4)	1.9112(3)	0.0227(3)	0.0262
9*K*-20*L*	0.8742(4)			
	0.8785(4)	0.8762(3)	0.0043(3)	0.0050
10*I*-30*K*	1.5388(3)			
	1.5599(3)	1.5485(2)	0.0211(2)	0.0230
10*K*-30*L*	0.6997(4)			
	0.7031(4)	0.7013(3)	0.0034(3)	0.0047

$$\Delta E_{c.g.} = \frac{(L+1)h\nu_- + Lh\nu_+}{(2L+1)} - \frac{\Delta E_{spin}(n_U)}{(2L+1)(2L+3)}. \quad (4)$$

This expression eliminates dependence on the calculated spin splitting in the (n_L, L) state, and the dependence on the splitting in the $(n_U, L+1)$ state, $\Delta E_{\mathrm{spin}}(n_U)$, is smaller than the experimental error bars in all cases and so is essentially negligible. Table III lists ΔE_{FS}, the inferred interval between the centers of gravity of each doublet, less the hydrogenic energy, for each measured transition.

C. Comparison with theory

The hope of extracting ion properties from fine-structure measurements in high-L, nonpenetrating Rydberg states rests on the relative simplicity of their fine structure and the possibility to characterize that structure precisely with a small number of parameters which represent properties of the free ion core. These ideas are not new [22–24], but they have been developed with increasing rigor as more precise experimental studies, and especially studies in Rydberg states of higher L, have appeared. The key idea is that, in many cases, there exists an "effective potential" whose expectation value over the Rydberg-electron wave function gives the fine-structure energy of any particular Rydberg state. The leading term in this potential for S-state ion cores is just the familiar adiabatic dipole polarization energy,

$$V_{eff}(r) \approx -\frac{1}{2}\frac{\alpha_1}{r^4} + \cdots, \quad (5)$$

where α_1 is the core ion's dipole polarizability and r is the radial coordinate of the Rydberg electron. This form would be expected to correctly describe the leading correction to the hydrogenic energy for a Rydberg electron moving very slowly and very far from the ion core. Of course, neither of these conditions is truly valid, and so many authors have considered how this simple idea could be modified to provide a more realistic description of the electron core interaction. Much of the early work on this question originated from workers interested in electron scattering, where similar questions appear. It is not obvious *a priori* that any potential can be found whose expectation value will accurately describe a wide range of Rydberg fine structures. Nevertheless, much more elaborate forms of this effective potential have been advanced over the years, including both higher-order adiabatic terms and several different forms of corrections for nonadiabatic effects in the interaction [25,26]. The study of Rydberg fine structure in the helium atom played an important role in these developments both because of its relative simplicity and because of the availability of precise measurements [27,28]. The most significant progress in helium, as measured by its impact on the general problem of Rydberg fine structure, is certainly the systematic development of the effective potential model by Drachman [29–32]. In a series of papers, Drachman showed rigorously that it was possible to formulate the helium fine-structure energies in terms of an effective potential containing increasing negative powers of r, and for this particularly simple core ion, he calculated the coefficients analytically for terms up to r^{-10}. His approach was quite formal, using the Feshbach projection operators to systematize the calculation. Ultimately, the utility of this approach is limited by the convergence of the asymptotic series represented by the effective potential, but the convergence improves as the angular momentum of the Rydberg state increases. For helium Rydberg states with $L \geqslant 7$ this approach gives higher precision than even the most precise calculations by more traditional methods [33]. A similar effective potential approach has been described by Laughlin in application to the Rydberg states of Ca, where the core ion is also an S state. This applies ideas very similar to Drachman's treatment of helium to the more general case, expanding on earlier ideas, which incorporate nonadiabatic corrections in other ways [34].

For the present purposes, it is not sufficient to simply cite these previous theoretical works since, as will be seen, they are not entirely adequate to describe our experimental measurements. In order to develop some insight into the possible reasons for this failure, it is helpful to present a less rigorous heuristic treatment of the effective potential model. The starting point for this model is the assumption of a zeroth-order description of the system in which the core ion and the Rydberg electron are completely independent. We take the Hamiltonian for the system to be given in atomic units by

$$H = H_0 + V,$$

$$H_0 = \left[\sum_{i=1}^{N-1}\left(\frac{|\vec{p}_i|^2}{2} - \frac{Z}{r_i}\right) + \sum_{\substack{i=1 \\ j>i}}^{N-1}\frac{1}{r_{ij}}\right] + \left[\frac{|\vec{p}_N|^2}{2} - \frac{Q}{r_N}\right],$$

$$V = \sum_{i=1}^{N-1}\frac{1}{r_{iN}} - \frac{(N-1)}{r_N} = \sum_{i=1}^{N-1}\sum_{k=1}^{\infty}\frac{r_i^k}{r_N^{k+1}}C^k(\Omega_i)C^k(\Omega_N), \quad (6)$$

where Z is the nuclear charge, N is the total number of electrons, and $Q=Z-N+1$ is the charge of the core ion. Clearly, H_0 describes the desired independent systems: the free core

ion and the hydrogenic Rydberg electron. Two important assumptions are embedded in this formulation: (1) The Rydberg electron, the *N*th electron, is assumed to be distinguishable from the core electrons. This is the justification for the asymmetric treatment of the *N*th electron in the Hamiltonian. (2) There is assumed to be no penetration of the core wave function by the Rydberg electron. This justifies dropping the scalar term in the interaction *V*. Less essential, perhaps, is the assumption of a nonrelativistic Hamiltonian for the core ion. However, it is convenient for this heuristic discussion. For simplicity, the electron spin is neglected in this discussion.

With this starting point, the energy of Rydberg states can be developed through perturbation theory. The zeroth-order wave functions are just products of core eigenfunctions (n_c, l_c) and Rydberg-electron functions (n, l), coupled to form total angular momentum L. For present purposes, we will assume that the core ion ground state has $l_c = 0$, and so the total angular momentum L is equal to the angular momentum of the Rydberg electron, l. For simplicity, we will denote the core ground state as $|g\rangle$. In zeroth order, of course, all Rydberg states of the same n are degenerate with this Hamiltonian. Note that the first-order perturbation in V vanishes for *S*-state core ions because of the assumption of nonpenetration. Clearly this limits the applicability of this approach to high-L Rydberg states. The first nonzero contribution to the fine structure, then, comes from the second-order perturbation in V,

$$E^{[2]}(g,nl;L) = -\sum_{\substack{n'_C,l'_C \\ n',l'}} \frac{|\langle g,(n,l);L|V|(n'_C,l'_C),(n',l');L\rangle|^2}{[E_C(n'_C,l'_C) - E_C(g)] + [E(n') - E(n)]}. \tag{7}$$

This expression can be further expanded in two other ways: First, the multipole expansion of the perturbation V divides $E^{[2]}$ into separate contributions from each multipole order. Second, the energy denominator in each term can be formally expanded in terms of the ratio of Rydberg to core energy differences, the "adiabatic expansion,"

$$\frac{1}{[\Delta E_{core} + \Delta E_{Ryd}]} = \frac{1}{\Delta E_{core}} - \frac{\Delta E_{Ryd}}{(\Delta E_{core})^2} + \frac{(\Delta E_{Ryd})^2}{(\Delta E_{core})^3} - \cdots, \tag{8}$$

$$\Delta E_{core} = E(n_c{}' l_c{}') - E(g),$$

$$\Delta E_{Ryd} = E(n') - E(n).$$

Substituting only the first term of this expansion into $E^{[2]}$ leads to the adiabatic polarization energies

$$E^{[2]}_{ad} = -\frac{1}{2}\alpha_1\langle r^{-4}\rangle_{nL} - \frac{1}{2}\alpha_2\langle r^{-6}\rangle_{nL} + \cdots, \tag{9}$$

where the brackets stand for radial expectation values in the Rydberg radial coordinate and

$$\alpha_1 = \frac{2}{3}\sum_{n'_c} \frac{[g\|r\|n'_c l_c = 1]^2}{(\Delta E_{core})},$$

$$\alpha_2 = \frac{2}{5}\sum_{n'_c} \frac{[g\|r^2\|n'_c l_c = 2]^2}{(\Delta E_{core})} \tag{10}$$

are the adiabatic dipole and quadrupole polarizabilities of the core ion. The square brackets above stand for radial integrals. In this limit, the Rydberg fine-structure energies are indeed the expectation value of an effective potential.

The nonadiabatic corrections to this picture have been dealt with in a number of ways by different authors, but the approach of Drachman amounts to substituting the second term of Eq. (8) into the expression for $E^{[2]}$ and using the properties of hydrogenic radial functions and integration by parts to express the result from the first two terms as

$$E^{[2]}_{ad+1stNA} = -\frac{1}{2}(\alpha_1\langle r^{-4}\rangle_{nl} - 6\beta_1\langle r^{-6}\rangle_{nl} + \cdots) - \frac{1}{2}(\alpha_2\langle r^{-6}\rangle_{nl} - 15\beta_2\langle r^{-8}\rangle_{nl} + \cdots), \tag{11}$$

where

$$\beta_1 = \frac{1}{12}\sum_{n'_c} \frac{[g\|r\|n'_c l_c = 1]^2}{(\Delta E_{core})^2},$$

$$\beta_2 = \frac{1}{20}\sum_{n'_c} \frac{[g\|r^2\|n'_c l_c = 2]^2}{(\Delta E_{core})^2}. \tag{12}$$

In this approach, the nonadiabatic corrections appear as higher inverse powers of r in the effective potential. Again the coefficients of the potential depend on only a few parameters, which are relatively simple properties of the free ion core. So the concept of an effective potential, independent of n and l, survives with this method. The influence of all possible core excited states is also naturally included with this approach. However, the method relies upon the convergence of the adiabatic expansion [Eq. (8)], which may be questionable when the core ion has low-lying excited states.

Incorporation of higher-order terms in perturbation theory, higher-multipole terms in V, and successive terms in the adiabatic expansion generates numerous additional terms in the expression above, all of which can be expressed in terms of a radial expectation value of a higher inverse power of the Rydberg radial coordinate. Of course, the utility of this formal expansion depends on the rapid convergence of the contributions from successive terms. The rate of convergence depends on the quantum numbers of the particular Rydberg state under study and especially on the angular momentum of that state, since this determines the inner turning point of the radial wave function. In practice, for any finite value of L, even if all the coefficients are known as in helium, successive terms begin to increase at some point, limiting the precision with which the fine-structure energy can be predicted. For the present purposes, the effective potential may be represented, to sufficient precision, by the first three terms,

TABLE IV. The relativistic ($\Delta E_{\rm rel}$) and second-order ($\Delta E^{[2]}$) contributions to each measured transition are shown in columns 2 and 3, respectively. $\Delta E^{\rm corr}$ is the measured interval $\Delta E_{\rm FS}$ corrected for the relativistic effects and second-order energies. The corrected interval is normalized to $\Delta\langle r^{-4}\rangle$ in column 5, and the calculated ratio $\Delta\langle r^{-6}\rangle/\Delta\langle r^{-4}\rangle$ for each transition is also given.

nL-$n'L'$	$\Delta E_{\rm rel}$ ($\rm cm^{-1}$)	$\Delta E^{[2]}$ ($\rm cm^{-1}$)	$\Delta E^{\rm corr}$ ($\rm cm^{-1}$)	$\Delta E^{\rm corr}/\Delta\langle r-4\rangle$	$\Delta\langle r-6\rangle/\Delta\langle r-4\rangle$
9*I*-17*K*	0.0005	0.0207	1.8900(3)	62.030(10)	$1.3888*10^{-3}$
9*K*-20*L*	0.0003	0.0035	0.8724(3)	61.921(21)	$6.1596*10^{-4}$
9*L*-20*M*	0.0002	0.0007	0.4211(3)	62.026(44)	$2.6645*10^{-4}$
10*I*-30*K*	0.0004	0.0170	1.5311(2)	62.172(8)	$1.4761*10^{-3}$
10*K*-30*L*	0.0003	0.0030	0.6980(3)	61.952(27)	$7.0577*10^{-4}$
10*L*-30*M*	0.0002	0.0006	0.3462(4)	62.005(72)	$3.4754*10^{-4}$
10*M*-30*N*	0.0002	0.0001	0.1820(5)	62.174(171)	$1.6442*10^{-4}$

$$V_{eff}(r) = -\frac{\alpha_1}{2}\frac{1}{r^4} - \frac{(\alpha_2 - 6\beta_1)}{2}\frac{1}{r^6} + \frac{A_8}{r^8}. \qquad (13)$$

The term proportional to r^{-8} is added as a stand-in for possible higher order terms, but most of our interest will be in the first two terms.

Two refinements must be made to this analysis before we can accurately treat the data. The first of these is especially significant when the dipole polarizability is large, as in the case of Ba^+. The most significant portion of the fourth-order perturbation in V is found to be equivalent to the action of V_{eff}, applied in second order in the space of Rydberg levels. This "second-order polarization energy" is simply a function of α_1, n, and L in the case where the scale of the fine structure pattern is largely determined by α_1, and it has been explicitly calculated for this case [35]. Given an approximate knowledge of α_1 for Ba^+, the second-order polarization energy can be calculated for each state of interest and subtracted from the observed intervals to obtain a result that can be compared directly to the expectation value of V_{eff}. The second refinement is accounting for the small relativistic contribution to the measured intervals, coming from the well-known "p^4" correction to the Rydberg-electron kinetic energy. These corrections are listed for each transition in Table IV. The fourth column lists the corrected fine structure intervals. These represent the difference of the fine structure energy of the lower state and the upper state, after subtracting the calculated contribution from relativistic effects and the second-order polarization energy. If the effective potential model describes the Rydberg fine structure accurately, these numbers should be equal to the difference of the expectation value of V_{eff} in the two states. In order to check this, the difference of hydrogenic radial expectation values in each pair of states can be computed, using the analytic expressions for the radial expectation values [36], corrected for finite core ion mass. The rough variation of the measured intervals can be removed by normalizing each measurement to the difference in the expectation value of r^{-4} in the two states, $\Delta\langle r^{-4}\rangle$. This produces values that are approximately constant, which would be expected to vary approximately linearly when plotted versus $\Delta\langle r^{-6}\rangle/\Delta\langle r^{-4}\rangle$. Figure 4 shows such a plot of the scaled intervals.

In order to determine the core polarizabilities from the measured transitions the data was fit to the following:

$$\frac{\Delta E^{corr}}{\Delta\langle r^{-4}\rangle} = A_4 + A_6\frac{\Delta\langle r^{-6}\rangle}{\Delta\langle r^{-4}\rangle} + A_8\frac{\Delta\langle r^{-8}\rangle}{\Delta\langle r^{-4}\rangle}. \qquad (14)$$

The A_4 parameter represents half the dipole polarizability, A_6 represents $1/2(\alpha_2 - 6\beta_1)$, and A_8 allows for the possibility of contributions from higher terms. One obvious problem occurs in carrying out this fit. There is no choice of the three parameters which will consistently fit all the data, including both the 9*I*-17*K* and the 10*I*-30*K* intervals. Regardless of this, the best choice of the intercept A_4 and the initial slope A_6 appears to be tightly constrained by the data pattern. This can be illustrated by excluding one or the other nI-$n'K$ intervals from the fit, resulting in the two smooth curves shown in Fig. 4. The resulting values of A_4 and A_6 are virtually identical in the two fits. The precise form of the curvature does not appear to be critical either, since when these two fits are repeated including a term proportional to r^{-7} instead of

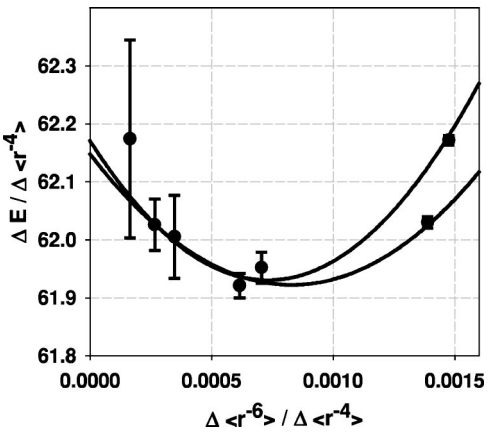

FIG. 4. The measured fine-structure intervals corrected for relativistic and second-order energy effects as described in the text and normalized to $\Delta\langle r^{-4}\rangle$ are plotted versus $\Delta\langle r^{-6}\rangle/\Delta\langle r^{-4}\rangle$. The solid lines indicate the fit to the data from the effective potential model excluding one or the other of the rightmost points, which correspond to exciting the 9*I* and 10*I* states.

the term proportional to r^{-8}, neither the intercept nor the initial slope is significantly altered. Taking into consideration the fitted values of A_4 and A_6 in all four of these fits, the best values are found to be

$$A_4 = 62.178(87),$$

$$A_6 = -828(260).$$

The dipole polarizability determined in this way is

$$\alpha_1 = 2A_4 = 124.36(17)a_0^3. \quad (15)$$

In order to extract a value for the quadrupole polarizability from A_6, we first need to determine β_1. To a very rough approximation this can be estimated by assuming that the dipole polarizability comes entirely from the lowest excited core state whose excitation energy (0.097 455 a.u.) is known. If this were the case, the value of α_1 found above and Eqs. (10) and (12) would imply that $\beta_1 = 645$ a.u.. This is an upper limit to the actual value since all other excited P states have larger excitation energies. For a more accurate estimation, the $6s-6p$ matrix element calculated by Dzuba *et al.* [15] can be used to find the lowest state contribution to the dipole polarizability. This turns out to contribute about 96% of the total. Based on this information and the value of α_1 obtained above, an improved estimate of β_1 is obtained which should be adequate for the present purposes. We take $\beta_1 = 583(20)a_0^5$, attaching a conservative estimate of error. As a result, the adiabatic quadrupole polarizability of Ba^+ is determined to be

$$\alpha_2 = 2A_6 + 6\beta_1 = 1842(533)a_0^5. \quad (16)$$

The lack of complete agreement between the measured intervals and the fit to Eq. (14) is still a cause for some concern. It appears to indicate that the effective potential model fails, even for states with $L=6$. The situation appears even worse when previous measurements of *nI*-*nK* and *nH*-*nI* intervals in $n=18$–21 [17] are included in the picture, as in Fig. 5. In this previous study a single *nG* state is prepared by a series of laser excitations and then excited to the final state by single and multiphoton microwave transitions. Two values are reported for each transition as a result of the spin splitting mentioned earlier. These give the positions of the two members of the spin doublet with respect to the original *nG* state. The indirect spin orbit theory [18] gives a sufficiently accurate description of the splittings that we can confidently state that the higher-energy state is the state with $K=L+1/2$. This information allows us to take a proper weighted average of the two level positions in the doublet to determine the center of gravity for each *nL* level, still with respect to the single *nG* level. Then the difference between these values for states with different L's can be taken to determine the $\Delta L=1$ intervals listed in column 2 of Table V as ΔE. As in the treatment of the new data discussed above, corrections were made to these measurements to account for relativistic effects and second-order energy corrections, and these are listed in Table V. Core penetration is not expected to be significant for states with $L \geqslant 5$, for which the inner turning point of radial motion is $15a_0$. Calculated estimates of penetration corrections for barium *nH* and *nI* states [37] suggest they may be marginally significant for the *nH*-*nI* intervals measured by Gallagher *et al.* [17]. Therefore those data are also corrected for these contributions, shown separately in Table V. Similar corrections are insignificant for higher-L intervals. The resulting corrected intervals are scaled and plotted along with the new data as solid points in Fig. 5. Also shown in Fig. 5 by solid lines are the extrapolated fit functions from Fig. 4. Not only do these functions fail to intersect or even closely approach the older data, but it is apparent that no choice of the parameters A_4, A_6, and A_8 could ever fit all the data, since a function of this form must monotonically change its slope. Thus, inclusion of the older data confirms that, while the effective potential model appears adequate for states with $L \geqslant 7$, it fails to describe measurements of states with $L \leqslant 6$.

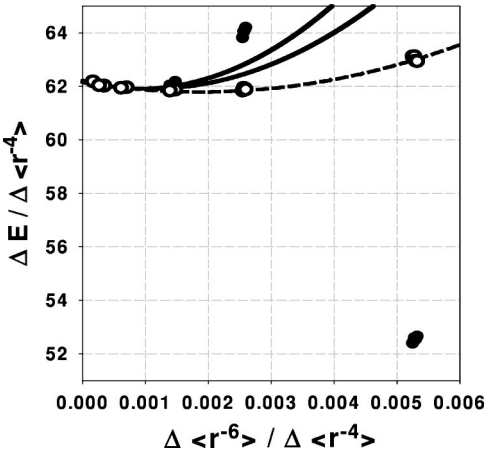

FIG. 5. The solid points less than 0.002 on the x axis and the two solid lines are taken from Fig. 4, while the solid points above 0.002 are the results from the previous study by Gallagher and co-workers [17]. Each of these points is scaled and plotted as in Fig. 4. Clearly, neither of the Fig. 4 fits is an adequate fit of all the data. The open points and the dashed line illustrate the quality of the fit to the modified potential model represented by Eq. (20) of the text. The term proportional to A_0 in Eq. (20) is not a smooth function of the x axis in this figure. Therefore to illustrate the fit we have subtracted from the data points the fitted contribution of this term, leading to the open points. These are then compared with the dashed line, which represents the best fit to Eq. (20), but again with the term proportional to A_0 excluded.

The complete pattern of data shown in Fig. 5 is in clear contrast to the expectations based on the effective potential model. It was for this reason that we presented the heuristic explanation of the assumptions underlying the model. The basic multipole expansion of the interaction seems secure. Certainly the weakest link in the assumptions is the use of the "adiabatic expansion" [Eq. (8)] to formally express nonadiabatic corrections to each multipole order of the second-order energy as successively higher inverse powers of r. The convergence of this expansion and of the potential derived from it depends of the relative size of the core and Rydberg energy differences. The dipole polarization energy is probably not a problem in this respect, since the excitation energy of the lowest P state of the core is about 2.6 eV. The quadrupole polarization energy, however, appears quite problematic since the lowest D state of the core ($5D$) is only about

TABLE V. Barium fine-structure intervals as determined by previous measurements of Ref. [17]. Column 2 gives the interval between the center of gravity of the two fine-structure levels listed in column 1, computed with the use of the indirect spin-orbit model. Relativistic, second-order energy, and core penetration contributions are listed and the resulting corrected energy interval is given as ΔE^{corr} in column 5. The normalized interval is listed in column 6 and with the calculated ratio $\Delta\langle r^{-6}\rangle/\Delta\langle r^{-4}\rangle$ in column 7.

nL-$n'L'$	Wtd. ave. ΔE (MHz)	ΔE_{rel} (MHz)	$\Delta E^{[2]}$ (MHz)	ΔE penetration (MHz)	ΔE^{corr} (MHz)	$\Delta E^{\mathrm{corr}}/\Delta\langle r-4\rangle$	$\Delta\langle r-6\rangle/\Delta\langle r-4\rangle$
18*H*-18*I*	10 910.7	0.9	620.5	17.9	10 271.4	52.394(8)	0.005 251
19*H*-19*I*	9330.2	0.7	529.7	15.5	8784.3	52.581(7)	0.005 278
20*H*-20*L*	8011.2	0.6	455.7	13.4	7541.5	52.549(6)	0.005 301
21*H*-21*I*	6944.7	0.5	394.8	11.7	6537.7	52.648(9)	0.005 321
18*I*-18*K*	4876.9	0.6	86.6	0.3	4789.4	63.811(23)	0.002 546
19*I*-19*K*	4174.4	0.5	74.1	0.3	4099.5	64.037(27)	0.002 565
20*I*-20*K*	3593.5	0.4	63.9	0.2	3529.0	64.124(29)	0.002 581
21*I*-21*K*	3114.9	0.4	55.4	0.2	3058.9	64.196(38)	0.002 595

0.6 eV above the ground state, and this is comparable to the energy differences between intermediate Rydberg states. The convergence of the adiabatic expansion of the quadrupole second-order energy therefore, which is assumed to obtain the effective potential, may be questionable. Fortunately, it is not difficult to check this point directly. The portion of the quadrupole second-order energy due solely to the lowest d state, the 5d state, can be isolated and directly compared with the approximation derived by retaining only the first two terms of the adiabatic expansion. The first part of this calculation is precisely the route followed by Gallagher *et al.* [17]. They introduced the correction factor k_Q, which relates the entire quadrupole second-order energy, due to this single-core excitation, as

$$E^{[2]}_{\kappa=2}(6^2S_{1/2},nl;L)_{5d\ only} \equiv -\frac{1}{2}k_Q\alpha_2^0\langle r^{-6}\rangle_{nL}, \tag{17}$$

where

$$\alpha_2^0 = \frac{2}{5}\frac{[6s|r_i^2|5d]^2}{E_{5d}-E_{6s}} \tag{18}$$

is the part of the adiabatic quadrupole polarizability due exclusively to the 5D state of the Ba^+ ion and

$$\begin{aligned} k_Q \equiv & \frac{3(E_{5d}-E_{6s})}{2(4L^2-1)(2L+3)\langle nL|r_2^{-6}|nL\rangle} \\ & \times\Bigg[(2L-1)(L+1)(L+2)\sum_{n'}\frac{[n'l+2|r_2^{-3}|nl]^2}{E_{5dn'}-E_{6sn}} \\ & +\frac{2(L^2+L)(2L+1)}{3}\sum_{n'}\frac{[n'l|r_2^{-3}|nl]^2}{E_{5dn'}-E_{6sn}} \\ & +(2L+3)(L^2-L)\sum_{n'}\frac{[n'l-2|r_2^{-3}|nl]^2}{E_{5dn'}-E_{6sn}}\Bigg]. \end{aligned} \tag{19}$$

We note that while Eq. (19) agrees with Ref. [17] it differs by a factor of 5 from that given in Ref. [38].

Once k_Q is computed in this way, it can be compared with the approximate form that would be obtained by retaining only the first two terms of the adiabatic expansion of the quadrupole polarization energy, again including only the 5d core excitation:

$$k_Q^{approx} = 1 - \frac{15}{E_{5d}-E_{6s}}\frac{\langle r^{-8}\rangle_{nL}}{\langle r^{-6}\rangle_{nL}}. \tag{20}$$

This comparison is shown in Fig. 6 for $n=10$ Ba Rydberg states with $6\leqslant L\leqslant 9$. In this case, the approximate form appears to be a reasonable first approximation of the nonadiabatic correction only for $L=9$. For states with $L\geqslant 7$ the first correction is at least much smaller than 1, suggesting that the series may converge and eventually approximate the full result. However, for $L=6$ the first correction term is nearly as

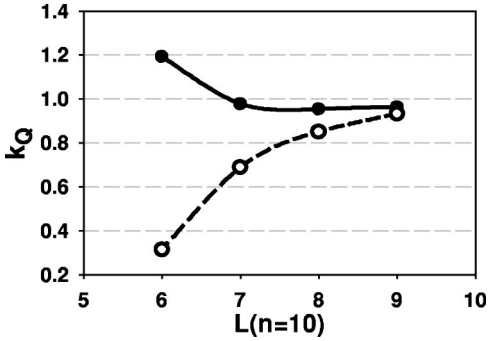

FIG. 6. The nonadiabatic correction factors k_Q calculated for $n=10$ barium Rydberg levels are shown by the solid points. The approximate values k_Q^{approx} determined from the first two terms of the adiabatic expansion [Eq. (20)] are shown as open points. In both cases, the difference of k_Q from one represents the nonadiabatic correction. Clearly, the accuracy of the approximate method increases with L, and inclusion of subsequent terms in the adiabatic expansion would be expected to improve the agreement further. However, for $L=6$, since the first correction in k_Q^{approx} is almost as large as 1 it seems unlikely that this approach to describing the nonadiabatic corrections can succeed for barium Rydberg states with $L\leqslant 6$.

large as the leading term, making the convergence unlikely. This indicates that the reason for the failure of the effective potential model in Fig. 5 is likely the inappropriate adiabatic expansion of the second-order quadrupole energy.

If indeed this is the reason for the discordant data pattern of Fig. 5, it may also suggest a better way to treat the data. There is no reason to doubt the convergence of the adiabatic expansion for whatever part of the quadrupole second-order energy is due to higher D states of Ba^+, which are at least 5.6 eV above the ground state. (This is easily confirmed by repeating the test of Fig. 6 after artificially expanding the $5d$ excitation energy.) It should be possible, therefore, to write a modified potential, whose expectation value should give the Rydberg fine-structure energy as

$$V_{pol}(n,L) = -\frac{\alpha_1}{2}\frac{1}{r^4} - \frac{(\alpha_2 - 6\beta_1)}{2}\frac{1}{r^6} - \frac{\alpha_2^0}{2}[k_Q(nL) - 1]\frac{1}{r^6} + \frac{A_8}{r^8} + \cdots . \quad (21)$$

In this expression, α_1, β_1, and α_2 have their usual definitions, and the term proportional to $(k_Q - 1)$ describes the entire nonadiabatic contribution to the part of the quadrupole second-order energy due to the $5d$ state. As indicated, since k_Q is a function of n and L, this is no longer a true effective potential. Nevertheless, since it avoids the convergence difficulties discussed above, it might give a better account of the data pattern. In order to test this, we fit the data to a function of the form

$$\frac{\Delta E^{corr}}{\Delta\langle r^{-4}\rangle} = A_4 + A_6\frac{\Delta\langle r^{-6}\rangle}{\Delta\langle r^{-4}\rangle} + A_0\frac{\Delta|(k_Q - 1)\langle r^{-6}\rangle|}{\Delta\langle r^{-4}\rangle} + A_8\frac{\Delta\langle r^{-8}\rangle}{\Delta\langle r^{-4}\rangle}. \quad (22)$$

The third term requires independent calculation of the k_Q factors for each level studied. The Appendix tabulates the values calculated for each of the levels of this study and describes the method used to calculate them, which differs in some respects from that used in the study of Gallagher *et al.* [17].

All of the data shown in Fig. 5 can be fit with Eq. (22), and this confirms our hypothesis that the failure of the effective potential model is due to the low-lying $5d$ state. In order to illustrate this fit in Fig. 5, the contribution of the term proportional to A_0 was subtracted from each point to obtain the open circle points in Fig. 5. Then a dashed curve corresponding to the remaining three terms in the fit function was added to show the quality of the fit. This appears to give a very satisfactory resolution of the difficulty initially presented by Fig. 5. Our conclusion is that the nonadiabatic corrections to the quadrupole polarization energies for states with $L \leqslant 6$ are very large and dominated by the contributions of the lowest core-excited d state, the $5d$ state. The excitation energy of this state is so small that the adiabatic expansion, used to derive the form of the effective potential, fails badly. However, it is possible to treat the part of the quadrupole polarization energy coming from the $5d$ state independently and to calculate a nonadiabatic correction factor k_Q for each Rydberg level studied. The remainder of the fine-structure energy is still described by an effective potential model and can be fit consistently in this way to extract core parameters. As in the fit of Fig. 4, we also repeated the fit of Fig. 5 data using a term proportional to r^{-7}, instead of proportional to r^{-8} and found little effect on the fitted values of A_4 and A_6. In both of these fits, to avoid giving excessive weight to the older data, which appeared internally inconsistent, the uncertainties for that data were arbitrarily expanded by a factor of 7. It was still necessary to expand the fitted parameter errors slightly to account for the excess scatter in the fit. For best fit values of A_4, A_6, and A_0, we quote the average of the results found in the two types of fit

$$A_4 = 62.152(74),$$

$$A_6 = -518(170),$$

$$A_0 = 914(44).$$

The fitted values of A_4 and A_6 are consistent with the values obtained from the fits of Fig. 4. The fitted value of A_0 implies a value for α_2^0, the $5d$ state contribution to the quadrupole polarizability,

$$\alpha_2^0 = 2A_0 = 1828(88). \quad (23)$$

Our conclusions about the parameters characterizing the Ba^+ core, as derived from the separate fits of Fig. 4 and 5, are very similar. They are summarized in Table VI.

TABLE VI. Values of core parameters derived from the fits of Figs. 4 and 5 and previous determinations of α_1 and α_2 from Ref. [17].

Quantity	Fig. 4 fit	Fig. 5 fit	Previous expt.
$\alpha_1(a_0^3)$	124.36(17)	124.30(15)	125.5(1.0)
$\alpha_2(a_0^5)$	1842(533)	2462(361)	2050(100)
$\alpha_2^0(a_0^5)$		1828(88)	

The previous measurements of α_1 and α_2 are also shown in Table VI. Comparison of our results with these measurements [17] is complicated by the different methods of data analysis. The previous study fit their measurements by assuming that

$$E^{[2]} = -\frac{1}{2}k_d\alpha_1\langle r^{-4}\rangle_{nl} - \frac{1}{2}k_Q\alpha_2\langle r^{-6}\rangle_{nl}, \quad (24)$$

where the factors k_d and k_Q are introduced to account for nonadiabatic corrections to the fine-structure energies. In both the dipole and quadrupole cases, these factors were calculated under the simplifying assumption that only one core excited state contributes to the polarizability. That is, only the lowest p state contributes to α_1 and only the lowest d state contributes to α_2. In the case of α_1, we now believe that the lowest p state contributes about 96% of the total dipole polarizability. The calculated nonadiabatic correction factors k_d are also close to 1, meaning that the nonadiabatic corrections are small [17]. The nonadiabatic corrections to the small portion of the dipole polarization energy coming from higher p states are certainly much smaller than the correc-

TABLE VII. Calculated values of the core parameters measured in this work. Column *A*: relativistic many-body perturbation theory (α_1), Dirac Hartree-Fock (α_2) [39]. Column *B*: model potential [40,41]. Columns *C*,*D*,*E*: Coulomb approximation (cited in Ref. [42]); column *F*, Hartree-Slater (cited in Ref. [42]).

Quantity	*A*	*B*	*C*	*D*	*E*	*F*
$\alpha_1(a_0^3)$	124	135	117.1	118.7	122.6	144.1
$\alpha_2(a_0^5)$	4240	4301	2245.1	2370.0	2589	3102.7
$\alpha_2^0(a_0^5)^0$	3268	2076				

tions to the dominant portion. Still, the error incurred by assuming that the calculated k_d applies to the entire polarization energy is not large, approximately 0.2%. Therefore it is not surprising that we find good agreement with the previously reported value of α_1 in spite of the different methods of analysis. Comparison with the previously reported value of α_2 is not as satisfactory. In this case the assumption that the correction factor k_Q, calculated by including only the lowest *d* state, can be assumed to apply to the entire quadrupole polarization energy is more seriously in error. This is partly due to the fact that the lowest *d* state contributes a smaller fraction of the total quadrupole polarization energy [74(11)% by our estimate], but also due to the fact that the nonadiabatic corrections are much larger. Consequently, the previous result underestimates α_2; our result is 1.20(15) times larger. The large nonadiabatic corrections to the quadrupole polarization energies play a dominant role in the data pattern, as illustrated in Fig. 5. For this reason, it is not surprising that the previous result is closer to our estimate of α_2^0, the portion of α_2 due exclusively to the 5*d* state, for which the nonadiabatic corrections are large.

Table VII collects previous theoretical calculations of the core polarizabilities measured here. For α_1, the calculated values range from 117 to 144. The result of Porsev and Derevianko, column *A*, using the relativistic many-body theory method is in excellent agreement with our measured result. This method is expected to provide the most accurate theoretical description of the Ba^+ ion. Unfortunately, it is not possible to compare with this calculation at the level of precision of the experiment because of the limited number of digits in the reported theoretical result. Agreement with calculations obtained with other methods is less satisfactory. Comparison with theoretical calculations of α_2 and α_2^0 are far less clear-cut. The results of Porsev and Derevianko, column *A*, who in this case report results with the Dirac-Hartree-Fock method [39], overestimate both properties by about a factor of 2, although the ratio of the two values is predicted correctly. The disagreement between experiment and theory for α_2^0 is particularly disturbing because of the importance of this particular matrix element in interpreting the proposed parity violation measurements in Ba^+ [11]. Agreement with some of the other calculations is somewhat better. For example, the calculation of Cohen, column *B*, shows better agreement for α_2^0, but still apparently overestimates α_2. Other calculations show better agreement for α_2, but do not report a separate value for α_2^0. We hope to improve the precision of this measurement and obtain a more decisive test of theoretical calculations by extending our study to higher-*L* levels using microwave methods.

IV. CONCLUSION

A factor of 6 increase in precision of the dipole polarizability of Ba^+ has been achieved through an optical RESIS study of high-*L* $n=9$ and 10 barium Rydberg states. An effective potential model used to describe the fine structure works for states of very high angular momentum, but in the case of barium begins to break down for $L<7$ states because of a low-lying core-excited *d* state. A modified effective potential model has been introduced and used to reconcile the fine-structure measurements of this work with older measurements, and this procedure also gives an independent determination of the portion of the quadrupole polarizability due to the 5*d* state, α_2^0. Good agreement with a recent theoretical calculation of α_1 is found, but agreement with calculations of α_2 and α_2^0 is rather poor.

ACKNOWLEDGMENTS

This work was supported by the Chemical Sciences, Geosciences, and Biosciences Division of the Office of Basic Energy Sciences, Office of Science, U.S. Department of Energy. We thank Samuel Cohen for helpful comments.

APPENDIX

In order to obtain the most accurate values of k_Q possible for use in the analysis of the data in this study, several improvements over the steps used in reference [17] were undertaken.

(1) Since the 5*d* state is actually split into two fine-structure states, the definition of k_Q was expanded to include this core fine-structure splitting. Including the core spin also means that there are two *nL* Rydberg levels with $K=L+1/2$ and $K=L-1/2$, with somewhat different second-order quadrupole energies. To compare with experimental data, we computed the weighted average of these two energies. Retaining the definition of k_Q as

$$E^{[2]}_{\kappa=2}(6^2S_{1/2},nl;L)^{K\ average}_{5d\ only} \equiv -\frac{1}{2}k_Q\alpha_2^0\langle r^{-6}\rangle_{nL}, \qquad \text{(A1)}$$

where

$$\alpha_2^0 = \frac{2}{5}\frac{\langle 6s|r_i^2|5d\rangle^2}{(E_{5d})_{c.g.}-E_{6s}}, \qquad \text{(A2)}$$

but including the 5*d* fine-structure energy in the perturbation denominators, we find

TABLE VIII. Calculated k_Q values using the Dalgarno-Lewis method and including the fine-structure energies of the Ba^+5D states. The results for nh states were modified to account for a quantum defect of 0.05 in the $5d4f$ and $5d5f$ states. The quoted values correspond to a weighted average of the values computed separately for the $K=L\pm1/2$ states.

	H	*I*	*K*	*L*	*M*	*N*
9		1.482	0.968	0.957		
10		1.225	0.986	0.959	0.968	
17			1.059			
18	−0.658	1.652	1.065			
19	−0.612	1.686	1.070			
20	−0.573	1.718	1.074	0.989	0.973	
21	−0.540	1.747	1.077			
30			1.097	0.998	0.979	0.975

$$k_Q \equiv \frac{3[(E_{5d})_{c.g.}-E_{6s}]}{2(4L^2-1)(2L+3)\langle nL|r_2^{-6}|nL\rangle}\left[\frac{2}{5}\left(f_+\sum_{n'}\frac{[n'l+2|r_2^{-3}|nl]^2}{E_{5d_{3/2}n'}-E_{6sn}}+f_0\sum_{n'}\frac{[n'l|r_2^{-3}|nl]^2}{E_{5d_{3/2}n'}-E_{6sn}}+f_-\sum_{n'}\frac{[n'l-2|r_2^{-3}|nl]^2}{E_{5d_{3/2}n'}-E_{6sn}}\right)\right.$$
$$\left.+\frac{3}{5}\left(f_+\sum_{n'}\frac{[n'l+2|r_2^{-3}|nl]^2}{E_{5d_{5/2}n'}-E_{6sn}}+f_0\sum_{n'}\frac{[n'l|r_2^{-3}|nl]^2}{E_{5d_{5/2}n'}-E_{6sn}}+f_-\sum_{n'}\frac{[n'l-2|r_2^{-3}|nl]^2}{E_{5d_{5/2}n'}-E_{6sn}}\right)\right], \quad \text{(A3)}$$

where

$$f_+ \equiv (2L-1)(L+1)(L+2),$$

$$f_0 \equiv \left(\frac{2}{3}\right)(L^2+L)((2L+1),$$

$$f_- \equiv (2L+3)(L^2-L)\left(\frac{2}{3}\right).$$

(2) To evaluate the sums occurring in the definitions of k_Q, we used the Dalgarno-Lewis method [43] so that our calculation consistently includes contributions from both discrete and continuum levels. This implicitly assumes that all the intermediate Rydberg levels are hydrogenic.

(3) For the $6snh$ states alone, where the perturbations by the $5d4f$ and $5d5f$ are significant, we included a quantum defect for these states only, using a value of 0.05, as indicated in a spectroscopic study of [44].

With these steps, we obtained the k_Q values shown in Table VIII for the states relevant to this study. Since our calculation necessarily evaluated the contributions to k_Q from intermediate Rydberg levels with $L'=l-2, l$, and $l+2$, it was possible to note that the most significant variation of k_Q with L and thus the most significant effect on the fine-structure intervals was found in the $L'=l-2$ channel. Thus, for example, the nonadiabatic effects on the fine structure of $6snh$ levels were mostly due to $5dn'f$ states.

[1] R. F. Ward, Jr., W. G. Sturrus, and S. R. Lundeen, Phys. Rev. A **53**, 113 (1996).

[2] W. G. Sturrus, E. A. Hessels, P. W. Arcuni, and S. R. Lundeen, Phys. Rev. A **44**, 3032 (1991).

[3] P. L. Jacobson, R. A. Komara, W. G. Sturrus, and S. R. Lundeen, Phys. Rev. A **62**, 012509 (2000).

[4] R. A. Komara, M. A. Gearba, S. R. Lundeen, and C. W. Fehrenbach, Phys. Rev. A **67**, 062502 (2003).

[5] R. A. Komara, M. A. Gearba, C. W. Fehrenbach, and S. R. Lundeen J. Phys. B **37**, S87 (2005).

[6] F. J. Deck, E. A. Hessels, and S. R. Lundeen, Phys. Rev. A **48**, 4400 (1993).

[7] P. L. Jacobson, R. D. Labelle, W. G. Sturrus, R. F. Ward, Jr., and S. R. Lundeen, Phys. Rev. A **54**, 314 (1996).

[8] W. G. Sturrus, E. A. Hessels, P. W. Arcuni, and S. R. Lundeen, Phys. Rev. A **38**, 135 (1988).

[9] S. C. Bennett and C. E. Wieman, Phys. Rev. Lett. **82**, 2484 (1999).

[10] J. E. Simsarian, S. Aubin, J. S. Grossman, L. A. Orozco, M. R. Pearson, G. D. Sprouse, and W. Z. Zhao, in *Parity Violations in Atoms and Polarized Electron Scattering*, edited by Bernard Frois and Marie-Anne Bouchiat (World Scientific, Singapore, 1999), p. 312.

[11] T. W. Koerber, M. Schacht, W. Nagourney, and E. N. Fortson,

J. Phys. B **36**, 637 (2003).
[12] J. E. Simsarian, L. A. Orozco, G. D. Sprouse, and W. Z. Zhao, Phys. Rev. A **57**, 2448 (1998).
[13] J. E. Simsarian, W. Z. Zhao, L. A. Orozco, and G. D. Sprouse, Phys. Rev. A **59**, 195 (1999).
[14] J. S. Grossman, L. A. Orozco, M. R. Pearson, J. E. Simsarian, G. D. Sprouse, and W. Z. Zhao, Phys. Rev. Lett. **83**, 935 (1999).
[15] V. A. Dzuba, V. V. Flambaum, and J. S. M. Ginges, Phys. Rev. A **63**, 062101 (2001).
[16] E. H. Pinnington, R. W. Berends, and M. Lumsden, J. Phys. B **28**, 2095 (1995).
[17] T. F. Gallagher, R. Kachru, and N. H. Tran, Phys. Rev. A **26**, 2611 (1982).
[18] E. L. Snow, R. A. Komara, M. A. Gearba, and S. R. Lundeen, Phys. Rev. A **68** 022510 (2003).
[19] *Handbook of Laser Science and Technology*, edited by M. J. Weber (CRC Press, Boca Raton, 1982), Vol. II.
[20] G. W. F. Drake, in *Atomic, Molecular, and Optical Physics Handbook*, edited by Gordon W. F. Drake (AIP, Melville, NY, 1996), p. 154.
[21] W. Vassen *et al.*, J. Opt. Soc. Am. B **6**, 1473 (1989).
[22] J. E. Mayer and M. G. Mayer, Phys. Rev. **43**, 605 (1933).
[23] E. S. Chang and H. Sakai, J. Phys. B **15**, L649 (1981).
[24] R. R. Freeman and D. Kleppner, Phys. Rev. A **14**, 1614 (1976).
[25] J. H. Van Vleck and N. G. Whitelaw, Phys. Rev. **44**, 551 (1933).
[26] C. J. Kleinman, Y. Hahn, and L. Spruch, Phys. Rev. **165**, 53 (1968).
[27] J. W. Farley, K. B. MacAdam, and W. H. Wing, Phys. Rev. A **20**, 1754 (1979); **25**, 1790(E) (1982), and earlier references therein.
[28] G. D. Stevens and S. R. Lundeen, Phys. Rev. A **60**, 4379 (1999), and earlier references therein.
[29] Richard Drachman, Phys. Rev. A **26**, 1228 (1982).
[30] Richard Drachman Phys. Rev. A **31**, 1253 (1985).
[31] Richard Drachman, Phys. Rev. A **37**, 979 (1988).
[32] Richard Drachman, Phys. Rev. A **47**, 694 (1993).
[33] G. W. F. Drake, in *Atomic, Molecular, and Optical Physics Handbook*, (Ref. [20]), p. 167.
[34] C. Laughlin J. Phys. B **28**, 2787 (1995).
[35] G. W. F. Drake and R. A. Swainson, Phys. Rev. A **44**, 5448 (1991).
[36] K. Bockasten, Phys. Rev. A **9**, 1087 (1974).
[37] Constantine E. Theodosiou, Phys. Rev. A **28**, 3098 (1983).
[38] T. F. Gallagher, *Rydberg Atoms* (Cambridge University Press, Cambridge, England, 1994), p. 372.
[39] S. G. Porsev and A. Derevianko (private communication).
[40] S. Cohen (private communication). Method is similar to that described in P. Camus and S. Cohen, Phys. Rev. A **51**, 1985 (1995).
[41] P. Camus and S. Cohen, Phys. Rev. A **51**, 1985 (1995).
[42] L. J. Curtis, P. S. Ramanujam, and C. E. Theodosiou, Phys. Rev. A **28**, 1151 (1983).
[43] A. Dalgarno and J. T. Lewis, Proc. R. Soc. London, Ser. A **233**, 70 (1955).
[44] E. A. J. M. Bente and W. Hogervorst, J. Phys. B **22**, 2679 (1989).